

3-dimensional kinematics in low foreground extinction windows of the Galactic bulge

Radial velocities for six bulge fields: procedures and results^{★,★★}

M. Soto^{1,3}, K. Kuijken¹, and R. M. Rich²

¹ Leiden Observatory, Leiden University, PO Box 9513, 2300RA Leiden, The Netherlands
e-mail: kuijken@strw.leidenuniv.nl

² Department of Physics and Astronomy, UCLA, Los Angeles, CA 90095-1547, USA
e-mail: rmr@astro.ucla.edu

³ Departamento de Física, Universidad de la Serena, Benavente 980, La Serena, Chile
e-mail: msoto@dfuls.cl

Received 15 January 2011 / Accepted 27 January 2012

ABSTRACT

Aims. The detailed structure of the Galactic bulge still remains uncertain. The strong difficulties of obtaining observations of stars in the Galactic bulge have hindered the acquisition of a kinematic representation for the inner kpc of the Milky Way. The observation of the 3-d kinematics in several low foreground extinction windows can solve this problem.

Methods. We have developed a new technique, which combines precise stellar HST positions and proper motions with integral field spectroscopy, in order to obtain reliable 3-d stellar kinematics in crowded fields of the Galactic center.

Results. In addition, we present results using the new techniques for six fields in our project. A significant vertex deviation has been found in some of the fields in agreement with previous determinations. This result confirms the presence of a stellar bar in the Galactic bulge.

Key words. Galaxy: bulge – Galaxy: kinematics and dynamics – Galaxy: structure

1. Introduction

The Milky Way bulge is the nearest example of a bulge/spheroidal population that we can observe. Its proximity allows us to resolve stellar populations and the associated kinematics, something which is not possible in external galaxies. Even though many data have been gathered, a detailed unified picture of the Galactic bulge including abundances, stellar populations and kinematics is far from being completed.

One of the main difficulties is the location of the Sun inside the disk dust layer, which limits observations to a few windows where the foreground dust extinction is relatively low. In addition, populations in these windows are projected on top of each other, complicating the analysis. Disk and bulge components overlap in the color–magnitude diagram specially near the turn-off (Holtzman et al. 1998), hampering a selection based on photometric criteria alone.

In spite of these limitations, important information has been gathered over the years. One of the pioneering studies of the

kinematics of the Galactic bulge was that of Spaenhauer et al. (1992), who measured proper motions for ~400 stars from photographic plates obtained in 1950 and 1983. This proper motion sample was the basis for subsequent abundance and radial velocity studies of the original proper motion sample (Terndrup et al. 1995; Sadler et al. 1996). Zhao et al. (1994) combined the results of these studies with those obtained previously by Rich (1988, 1990), and compiled a small subsample of 62 K Giants with 3-d kinematics and abundances. In spite of its small size the subsample showed a significant vertex deviation, a signature of barlike kinematics. This result has recently been confirmed with a larger sample of ~300 stars (Soto et al. 2007). de Vaucouleurs (1964) had originally suggested that our Galactic bulge was actually barred, based on the similarity of its spiral structure with other galaxies with strong bars. Nevertheless, direct stellar signatures of the barlike structure had not been found before. Other studies have also produced important kinematic catalogs for the regions at the center of our galaxy. Sumi et al. (2004) used the information provided by the OGLE catalog to produced 5×10^6 stellar proper motions in 49 bulge fields. The latter results have been the basis of a study of proper motion trends in the Red Clump of the bulge region (Rattenbury 2007a,b). The Rattenbury et al. (2007a) selection, however, seems to have suffered from a significant disk contamination as pointed out by other authors (Vieira et al. 2007). Plaut's Window ($l, b = 0^\circ, 8^\circ$) has also provided proper motions (Vieira et al. 2007), which have been obtained with plate observations spanning 21 years

* Based on observations collected at the European Organisation for Astronomical Research in the Southern Hemisphere, Chile. European Southern Observatory (ESO) programme numbers 71.B-3048(A), 077.B-0600(A) and 079.B-0232(A).

** Based on observations made with the NASA/ESA Hubble Space Telescope, obtained at the Space Telescope Science Institute, which is operated by the Association of Universities for Research in Astronomy, Inc., under NASA contract NAS 5-2655. These observations are associated with proposals GO-8250, GO-9436, GO-9816 and GO-11655.

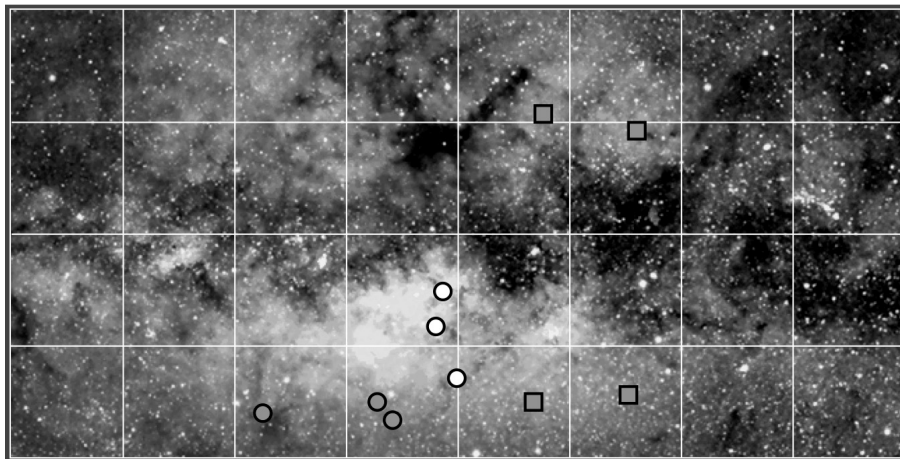


Fig. 1. Fields in the Galactic bulge observed for this project, superimposed on an optical map (Mellinger 2008), from longitude $+20^\circ$ to -20° , and latitude -10° to $+10^\circ$. White and grey circles correspond to fields for which proper motion and radial velocity measurements have been completed. Data sets for the four fields at negative longitudes (grey squares) have not been completed so far.

of epoch difference. Bulge stars in these fields have been selected by cross-referencing with the 2MASS catalog in order to obtain a clean sample of bulge giants. More recently, Clarkson et al. (2008) has produced a new catalogue of $\sim 180\,000$ proper motion using two ACS epochs; from this sample $>15\,000$ bulge proper motions were identified using a kinematic selection.

In addition to models of the stellar distribution (e.g. Zhao 1996) gas observations and hydrodynamical models also have been used to study the Galactic bulge (e.g. Englmaier & Gerhard 1999). Many of these models rely on three dimensional deprojections of the Galactic bulge derived from the COBE DIRBE images (Dwek et al. 1995) whose results showed asymmetries consistent with a stellar bar in the Galactic center. Even though all analyses agree on the rough orientation of the bar, complete agreement about the values of the parameters which would define this bar, such as rotational bar pattern speed or position angle has not been reached yet. For example, values for the angle between the bar's major axis and our line of sight to the Galactic center have ranged from $\sim 10^\circ$ (e.g. Picaud & Robin 2004, and references therein) to 80° (Collinge et al. 2006). Furthermore, the presence of 2 bar structures coexisting in the Galactic bulge has been proposed by some authors (Cabrera-Lavers et al. 2008, and references therein); the two more common bar angles ($\sim 20^\circ$ and $\sim 40^\circ$) belonging to 2 distinct triaxial structures, a boxy bulge/bar and a more extended long bar respectively. Nevertheless, this general picture with two bars rotating at different angles is dynamically complex (Martinez-Valpuesta & Gerhard 2011), and therefore is still under debate.

Similarly, the recent discovery of two coexistent red clumps in the Galactic bulge on 2MASS and OGLE-III data (McWilliam & Zoccali 2010; Nataf et al. 2010) and observed at high latitudes, has been interpreted as the effect of an X-shaped structure in the bulge (Saito et al. 2011). Hence, all this evidence suggest a complex bulge structure with several components detected at different lines of sight.

Understanding the bulge kinematics requires understanding the gravitational potential that drives the orbits (Kuijken 2004, henceforth K04). Once the kinematics are understood, they can be correlated with stellar population information to build a picture of the galaxy evolution and bulge formation scenario.

In order to improve our knowledge of the stellar kinematics in the bulge region we have embarked on a project to obtain three-dimensional velocities for a large sample of bulge stars,

by combining HST proper motions measurements with VIMOS spectroscopy.

In this paper we present integral-field (IFU) spectroscopic measurements for six bulge fields that have HST proper motion measurements: three fields on the minor axis (Kuijken & Rich 2002, henceforth KR02; KR04) as well as three fields at positive longitudes. We have combined the IFU data cubes with photometric information in a new procedure designed to work in crowded fields; the technique combines the precise HST photometry and IFU spectroscopy to optimize the spectral extraction.

Stellar kinematics involves measuring the phase-space distribution function. This phase space generally has three degrees of freedom. By providing 4–6 coordinates per star (the two proper motions, two sky coordinates, a distance determination by means of a main sequence photometric parallax, and a radial velocity for a subsample of bright stars) we can overconstrain the phase-space distribution which will allow us a reliable determination of the orbit structure.

The outline of this paper is as follows. In Sect. 2 we will briefly explain the project of which the work presented in this paper is a part, Sect. 3 is an account of the observations and the methods involved in each case. Section 4 contains the results of our analysis. Finally Sect. 5 is the summary and conclusions for this work.

2. Project

The *Hubble* Space Telescope (HST) data archive contains a treasure in WFPC2 images taken during the 1990s. This wealth of images can be used to find suitable first epoch fields for proper motion work; we have chosen ten for this project, with low foreground extinction, sufficiently deep exposures, and spread in l and b . Hence, the HST archive has provided us with first epoch observations in six fields at $l \sim 0$, and $l > 0$; in addition, we have established four fields at $l < 0$ in order to target both ends/sides of the bar/bulge. The goals for each field are the acquisition of color magnitude diagrams, accurate astrometry, and radial velocities for as many stars as possible.

Figure 1 shows all the fields for this project. HST archive images were primarily used to set first epoch proper motion exposures in several low extinction bulge regions, close to the Galactic minor axis and at positive longitudes. These initial

Table 1. Radial velocity and proper-motion fields.

Field	PM epoch	PM instrument	(l, b)	α, δ (J2000.0)
Sgr-I	1994 Aug.	WFPC2	(1.26, -2.65)	17 59 00, -29 12 14
	2000 Aug.	WFPC2		
Baade's Window	1994 Aug.	WFPC2	(1.13, -3.76)	18 03 10, -29 51 45
	1995 Sep.	WFPC2		
	2000 Aug.	WFPC2		
NEAR NGC 6558	1997 Sep.	WFPC2	(0.28, -6.17)	18 10 18, -31 45 49
	2002 Aug.	WFPC2		
Field 4-7	1995 Jul.	WFPC2	(3.58, -7.17)	18 22 16, -29 19 22
	2004 Jul.	ACS/WFC		
Field 3-8	1996 May	WFPC2	(2.91, -7.96)	18 24 09, -30 16 12
	2004 Jul.	ACS/WFC		
Field 10-8	1995 Sep.	WFPC2	(9.86, -7.60)	18 36 35, -23 57 01
	2004 Jul.	ACS/WFC		

fields were complemented more recently with observations in four more fields at negative longitudes. Thus, this project strategically spans a wide range of bulge locations, sampling a significant stellar population at the center and both sides of the bulge/bar. Consequently, the proper motion results published in KR02 and K04, represent the first important piece of kinematic information on this project, which we continue here. The complete HST programme described before, which points to proper motions, photometry and parallax distances has been more recently combined with a spectroscopic VLT programme in the same fields, this spectroscopic information, and the techniques involved are the subject of this paper, where Table 1 shows the coordinates of each field.

3. Observations and procedures

3.1. Proper motions

First epoch photometric observations with WFPC2 for all the fields used in this paper were obtained from the HST data archive. In the case of the three fields close to the Galactic minor axis (near $l = 0^\circ$) second epoch observations over a time baseline of 6 years have resulted in accuracies better than 1 mas/yr, which corresponds to errors below 30 km s^{-1} at the distance of the bulge, significantly smaller than the velocity dispersion of the bulge of 100 km s^{-1} . Even longer time baselines for the fields at positive longitudes were used (8–9 years) as Table 1 shows. First and second epochs were taken with WFPC2 for fields close to the Galactic minor axis, conversely fields at positive longitudes used a combination of WFPC2 and ACS for first and second epoch respectively. The latter fields thus had to include small differences in the procedure to take into account the instrument change (e.g. the shearing of ACS images with respect to WFPC2).

Proper motions were measured using a modification of the Anderson & King (2000) procedure, which consists of a combination of PSF reconstruction and PSF core fitting (KR02). A more detailed account about the proper motion measurements can be found in KR02 and it will not be repeated here.

3.2. Radial velocities

The procedure to obtain the spectrum of each star in these crowded fields consists of two main steps, the extraction of the spectra for each fiber/pixel in the IFU field, and the extraction of the star spectra from the IFU data cube. During the second step we will combine the spectroscopy with the information yielded by HST imaging.

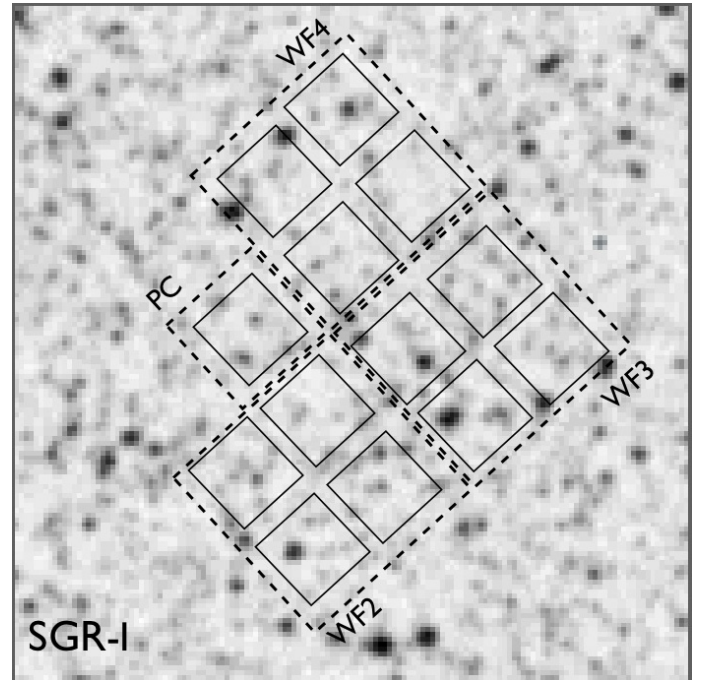


Fig. 2. Finding chart for one of our fields, *Sagittarius-I*, using an image from 2MASS. Each small square (solid line) corresponds to each one of the VIMOS IFU fields. Dashed squares correspond to PC, WF2, WF3 and WF4 HST fields superimposed on the same image.

The VLT VIMOS Integral Field Unit (IFU) has a $27'' \times 27''$ field of view in high resolution ($R \sim 2050$) which allows spectra to be taken on a 40×40 grid, of spacing $0.67''$. This permits spectroscopy of a large number of bulge stars in a single exposure, at a resolution of $0.54 \text{ \AA}/\text{pixel}$ from 4150 to 6200 \AA . We used this instrument to target our HST fields, which can each be covered by 13 VIMOS pointings (4 per WF chip and 1 per PC, as Fig. 2 illustrates for *Sagittarius-I*). Each IFU pointing was exposed for $2 \times 1000 \text{ s}$, which has allowed us to resolve approximately 80 stars per IFU field. The spectra yield 30 km s^{-1} radial velocity precision, which is well-matched to the transverse velocity accuracy from our proper motions (better than 1 mas/yr, equivalent to $\sim 30 \text{ km s}^{-1}$ at 8 kpc distance), and sufficient to resolve the velocity dispersion in the central parts of the Galaxy, which is about 100 km s^{-1} .

In addition to the regular science images containing the information about our six HST fields, we also made observations of highly extinguished bulge fields for use as “sky” exposures.

Table 2. Summary of radial velocity observations.

Field	1st run (2003)	2nd run (2006)	3rd run (2007)	Total IFU fields	Stars with rad. vel.
Sgr-I	5	6	5	16	962
Baade's Window	5	5	4	14	965
NEAR NGC 6558	5	5	4	14	766
Field 4-7	0	8	3	12	664
Field 3-8	0	10	3	13	466
Field 10-8	0	9	4	13	756

Standard stars were observed as well, for use as templates in the cross-correlation process for the determination of the velocities. The overall observation time for all the spectral observations was 17, 50 and 45 h for our three observing runs respectively. Table 2 summarizes the VIMOS IFU observations for the six fields presented in this paper. In Table 2 the numbers under every “run” column correspond to the number of IFU fields observed in that run. All data was taken in service mode with seeing conditions constrained at a maximum of $0.8''$.

3.2.1. Data cube organization and radial velocity measurements

VIMOS IFU raw data are complex to reduce and calibrate. Fiber spectra extraction was carried out using the ESO pipeline for VIMOS IFU data. Programs GASGANO¹ and ESOREX² were used to manage the VIMOS IFU recipes³ (Details about methods and procedures of the recipes can be found in VIMOS pipeline User's Guide and Gasgano User's Manual). The recipes used during our processing were *vmifucalib* and *vmifuscience*.

The final product of the VIMOS IFU recipes are the spectra extracted and wavelength calibrated in one image that includes all the spectra for each quadrant in the IFU field.

An important problem to be considered in spectroscopic reduction is related to the sky subtraction, which has not been implemented by the VIMOS pipeline (VIMOS Pipeline User's Guide 7.23.11). We have tried two approaches. The first is basically the same recommended by the VIMOS Pipeline User's Guide. We took the 20 spectra with lowest signal per quadrant (which means 5% of the total) and averaged them (taking care to reject the dead fibers). The combined spectrum was considered as sky and subtracted from the rest of the fibers. This way of proceeding is not ideally suited to crowded fields and could change the results by subtracting a flux level too high (or too low) from the reduced spectra. The second method involves exposures of nearby highly extinguished “dark bulge” fields, whose spectra, appropriately scaled, mimic the sky contribution to the stellar fields as Fig. 3 shows.

Both processes were extensively tested to check their influence on our radial velocity results; we found no significant differences for both procedures, typically below 3 km s^{-1} in the final velocity measurements per fiber. Given the reliability of our extraction we have preferred to use the sky extraction by dark fields in our fields.

Once the spectra were reduced we assembled them into spectral data cubes. In addition to the regular calibrations, we

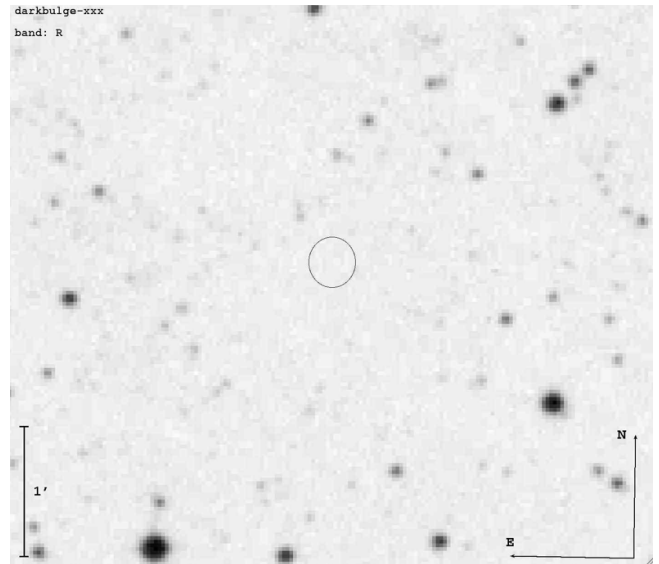


Fig. 3. Finding chart of one of our darkbulge fields (circle in the middle) over a 2MASS image. Darkbulge fields have been used during the sky subtraction in VIMOS IFU fields.

produced for each IFU field, a response map to check the normal behavior of the fibers through the field. Dead fibers or lost traces are easily highlighted in this way.

The last step is the radial velocity measurement per fiber in each IFU field. The measurement of radial velocities was made in all cases with a cross correlation in the IRAF⁴ task *fxcor* (Tonry & Davis 1979) against a template standard star (HD157457). Our template star has a Spectral type G8III, and therefore we expect a negligible bias favoring similar spectral types. Before the cross correlation some zones of the spectra were masked; for instance the atmospheric emission line due to OI at 5577.5 \AA ; or the interstellar absorption NaD lines at 5889 \AA . The latter lines are particularly strong in K2-3 III Giants, and can easily bias the correlation with our template to calculate velocities or a possible spectral type classification. An example of the velocity field calculated with the procedure here described for one of our IFU fields in Baade's Window appears in Fig. 4, and clearly shows distinct colored zones which correspond to different stars at different velocities. Extracting this information optimally is the subject of the next section.

¹ Available at <http://www.eso.org/sci/software/gasgano/>

² Available at <http://www.eso.org/sci/software/cpl/esorex.html>

³ Available at <http://www.eso.org/projects/dfs/dfs-shared/web/vimos/vimos-pipe-recipes.html>

⁴ “IRAF is distributed by the National Optical Astronomy Observatories, which are operated by the Association of Universities for Research in Astronomy, Inc., under cooperative agreement with the National Science Foundation”.

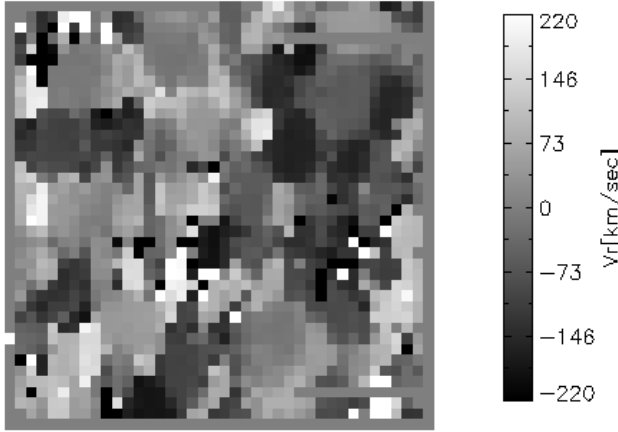


Fig. 4. Velocity field for one of our IFU observations in Baade’s window. The velocity for each pixel/fiber has been calculated using cross-correlation, where each fiber corresponds to $0.66''$. The VIMOS-IFU instrument allows clearly to distinguish between adjacent stars with different kinematics.

3.2.2. Deconvolution

As shown in Fig. 5, the bulge fields are very crowded, and therefore, a reliable technique to correct IFU spectra cubes for blending is absolutely necessary. Fortunately, our HST images allow us to know precisely where the stars are. This information makes feasible the optimal extraction of star spectra from the IFU cubes.

The first step to carry out the deconvolution process is a coordinate transformation from HST to IFU coordinates, which is performed using the standard IRAF tasks *daofind* and *geomap*. Since not all the stars observed in the HST image are detected in the IFU field, a threshold magnitude for the HST list stars must be given. In the case of the fields Sgr-I, and BW, for which we have F555W observations, this limiting magnitude was set at $V(F555W)_{\text{lim}} = 21$ mag. Similarly, for fields NEAR NGC6558 (which is actually located close to NGC 6558), Field 4-7, Field 3-8, and Field 10-8 the limiting magnitude is $V(F606W)_{\text{lim}} = 20\text{--}20.5$ mag, depending of the particular crowding in the IFU field. Using this limiting magnitude we avoid the deconvolution of the complete list of stars detected in the HST image, where naturally a large fraction of them are beyond the detection limit of the VIMOS IFU observations.

Armed with a magnitude-limited list of HST proper motions, positions, and magnitudes, we have produced a procedure which accounts for defects in the HST list to separate the fluxes of as many stars as possible from the VIMOS IFU spectral cube. Thus, the HST list, once cleaned from spurious stars due to failures in the DAOFIND detection procedure at 20σ , is used to perform the deconvolution of the stellar spectra in the IFU cube. The deconvolution requires a precise IFU PSF and the HST positions in the IFU field. Simultaneously, a convolved image using the HST magnitudes and positions and the IFU PSF is created during the deconvolution process. This convolved image yields an estimation of blending for each star which is used to select stars with a limited amount of blending for the final list of stars with radial velocities after the deconvolution. Hence, once stars have been deconvolved from the IFU-cube from a HST cleaned list, we can measure our radial velocities.

This deconvolution procedure can be described in more detail as follows: with the final list of cleaned HST stars lying in the

respective IFU field and the PSF of the latter we can estimate the contribution of a star s to each pixel i , which defines the model,

$$P_i = \sum_s F_s C_{si}, \quad (1)$$

where P_i is the flux in each pixel, F_s is the flux in the star s and C_{si} corresponds to the contribution of that star s to the pixel i obtained using the IFU PSF,

$$\chi^2 = \sum_i (P_i(\text{observed}) - P_i(\text{model}))^2 \quad (2)$$

$$= \sum_i (P_i(\text{observed}) - \sum_s F_s C_{si})^2, \quad (3)$$

which can be solved by requiring

$$\frac{\partial \chi^2}{\partial F_s} = 0 \quad \forall s. \quad (4)$$

This results in the matrix showed in Eq. (5)

$$\sum_{s'} F_{s'} \left(\sum_i C_{si} C_{s'i} \right) = \sum_i P_i C_{si}, \quad (5)$$

which defines a square system. The solution of this matrix for each slice of the IFU data corresponds to the flux solution to that wavelength for each star; repeating the procedure in every slice of the cube we are able to reconstruct the spectrum of each star.

This technique, simple in theory, might yield a singular matrix in some cases, when stars are too close to each other in the HST image, and therefore can not be resolved in the IFU image. Furthermore, saturation and bleeding would augment the probability of obtaining a singular matrix in Eq. (5), as these effects produce multiple DAOFIND detections around saturated spots. In order to avoid a singular matrix during the deconvolution procedure, we have implemented several solutions, which we describe below: (1) due to the differences in the pixel scale and resolution between the HST WFPC2 and the VIMOS IFU image (pixel scale is $0.046''$ for PC, and $0.1''$ for WF, while each pixel/fiber is $0.66''$ in VIMOS-IFU) it is expected that in many cases more than one HST star will fall in one single IFU pixel. Even in those cases, the fluxes of two stars in the same IFU pixel can be separated as long as they can be resolved as single stars using the IFU PSF and the HST positions. The IFU PSF has a typical FWHM in our observations of 1.8 pixels. Thus, we have found realistic to set a minimum blending radius for the stars in the HST list, stars closer than 0.01 IFU pixel-scale have been considered as one during the deconvolution, where fluxes have been added in those cases; (2) similarly, false detections due to bleeding and saturation in the HST list are discarded by comparing with the positions of stars in the IFU field. We cross matched both lists, identifying the HST star position which is closer to the position detected in the IFU field, and discarding the rest of the detections in the HST list inside an avoidance radius. Typically an avoidance radius of $0.5 \times \text{FWHM}$ of the IFU PSF has been used; (3) nevertheless, in spite of the two procedures just described, false DAOFIND detections in the HST list have eventually appeared during the deconvolution. These false stars in the HST list were particularly common in long exposures, where saturation and bleeding in bright stars left saturation many pixels away of the central position of the star. In order to solve this we have devised a simple local procedure which iteratively compares the convolved image generated by the HST position, magnitudes, and the IFU PSF with the real IFU field image; stars in

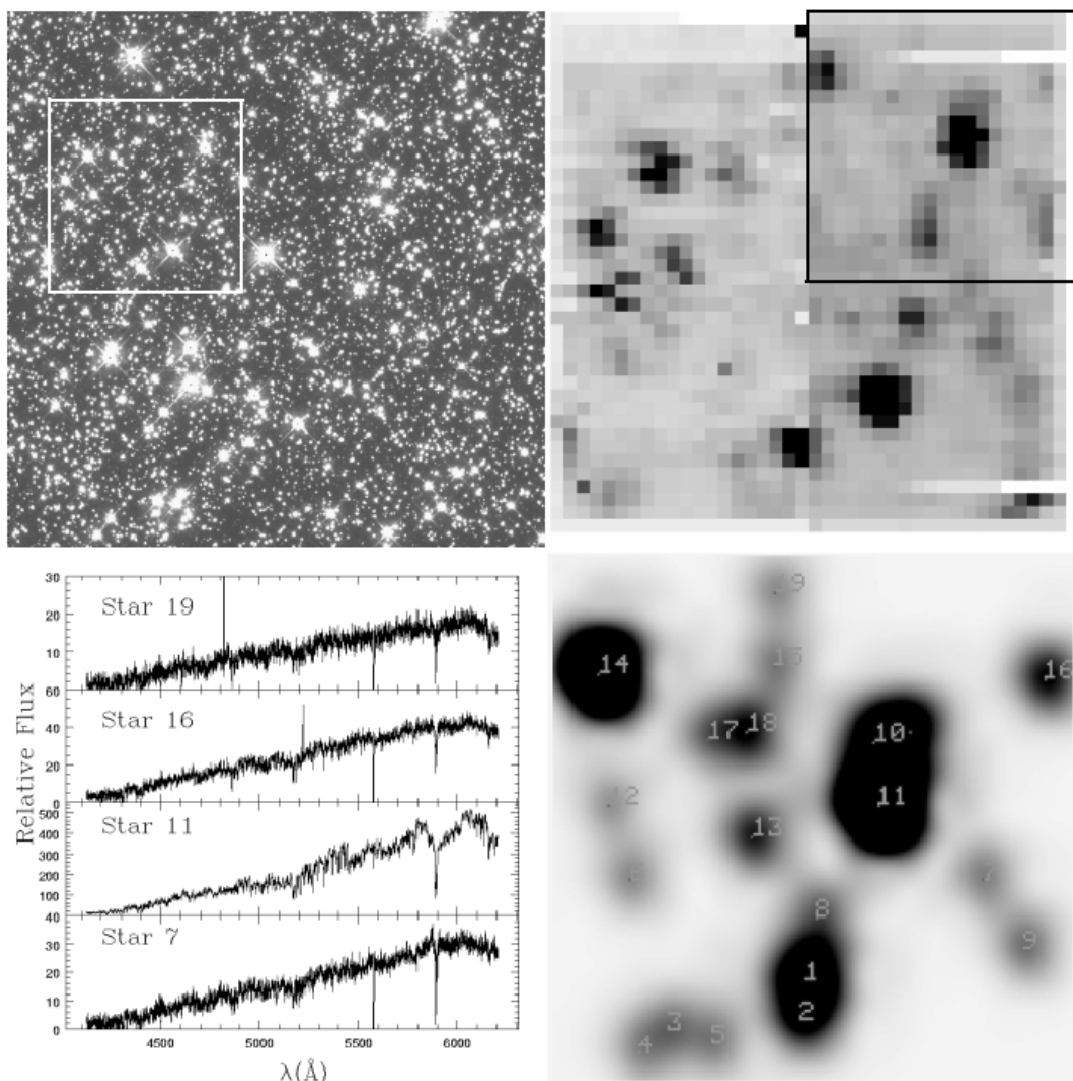


Fig. 5. Steps during the process to build a star spectrum from the spectral cube. The *top left* figure corresponds to one of our observations with HST WF2 in Baade’s window, the white square corresponds to the area covered by one of the VIMOS IFU images (*top right*). In the IFU field the first quadrant is enclosed, its respective convolved image produced during the deconvolution process to check the detection of stars in the first quadrant appear at the bottom right. Finally some examples of the spectra extracted by this process are shown at the bottom left.

the HST list with fluxes $2 \times$ background of a ratio image (real IFU image divided by a simulated IFU convolved image) are rejected and marked as false stars to generate a new convolved image and a new loop. This iterative process rapidly converges and effectively cleans of false stars due to saturated pixels the HST list of stars; (4) finally, once the deconvolution is performed, a final selection is carried out, as we mentioned before. This last selection is intended to avoid stars blended and/or mixing different populations which due to our radial velocity measurement technique, would deliver an average velocity as a result. Hence, we measure as many velocities as possible in single stars. Only stars in which the central positions had at least 70% of the total flux of the pixel were finally selected. Typical S/N for stars with radial velocity errors below 50 km s^{-1} was ~ 2.4 between 4500 \AA and 6000 \AA . An example of this process and its results is illustrated in Fig. 5.

A limitation of our technique is related to the PSF construction. The IFU field is small as we have already mentioned, which combined with the area covered for each fiber ($0.66''$), allows

only a few detections in each IFU exposure ($\sim 40\text{--}80$ typically, in normal conditions, with the four quadrants working). This small number of detections often produces a heavily undersampled PSF, which is critical in the deconvolution, where this PSF is used as a model to estimate the flux of every star.

During the development of our procedure each PSF was carefully obtained. The result of using a wrong PSF produces a flux overestimation of some stars. The result of this overestimation is negative fluxes in stars in the neighborhood of some bright stars which when projected to all the wavelengths in the spectral cube corresponds exactly to the spectrum of the neighbor bright star inverted as it is shown in Fig. 6. A similar result is obtained when many HST positions are located in the proximity of a very bright star, which is a typical failure of photometric detection in bright saturated stars. In all these cases it is not possible to obtain a reliable radial velocity measurement for these inverted spectra. Limited solutions implemented in our code, and already described, relate and compare the stars detected in the HST and VIMOS IFU field in order to solve the crowding. The

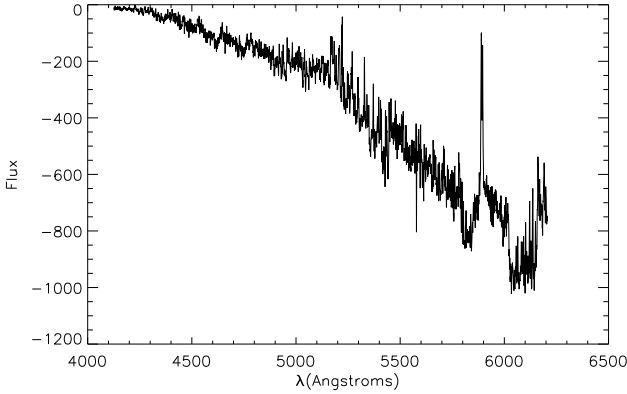


Fig. 6. Example of the result of using a wrong PSF during the deconvolution. This is the deconvolved spectrum for the HST position in the star 11 in Fig. 5 obtained using a modified PSF. The flux overestimation in a neighbor star by the PSF produces, when the system is solved, a negative solution for this star. A correlation can not be established with these distorted spectra in the radial velocity measurements.

undersampling of the IFU PSF on the other hand requires additional information. In order to improve this undersampled IFU PSF we performed, a Gaussian “refitting” of the IFU PSF generated by IRAF tasks, where several PSF models were tested. The PSF fit gives more weight to central pixels, where differences in background flux between original and refitted PSF were typically of the order of 3% and did not show significant consequences in the final velocity results. An example of the latter procedure is shown in Fig. 7, and a summary of all radial velocity measurements for our the six fields is indicated in Table 2.

Saturation not only affected our deconvolution procedure by adding false stars in the HST DAOFIND, also it affected the estimation of the amount of blending, and therefore the final selection of stars in the IFU spectral cube. The problem of saturation affecting the values of the magnitudes, was specially significant in NEAR NGC 6558 and the three off-axis fields, which count with first epoch HST observations originally intended for the study of faint stars, and therefore with long exposure times. The latter problem was partially solved with the calculation of *m814* aperture photometry magnitudes from short exposures (50 s) of the ACS second epoch images. This was possible only for the three off-axis fields Field 4-7, Field 3-8, and Field 10-8. Consistency of the velocity results has been checked using both magnitudes, showing no differences and therefore allowing us to avoid many misidentifications, after the deconvolution in these fields.

3.2.3. An alternative deconvolution

Since deconvolution and cross-correlation are both linear operators, they can be carried out in any order. Thus, an equivalent procedure to deconvolve the cross-correlation function (CCF) obtained from the velocity measurements of all fibers in the quadrant has been implemented. The procedure separates the contributions of the flux of each star in each pixel in the CCF data cube in the same way that spectra for all the stars are deconvolved from the spectra data cube. Consistency between the velocity results using both methods has been tested in the VIMOS field Baade’s Window WF2c. We have measured an average modulus difference for this field of $7 \pm 8 \text{ km s}^{-1}$ which we attribute mostly to small differences in the fitting of the CCF.

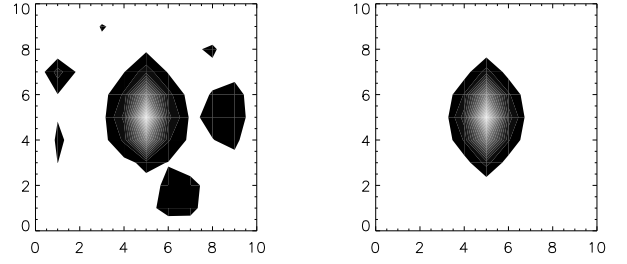


Fig. 7. Example of procedure to “refit” a IFU PSF. The undersampling of the IFU PSF is fixed by a new fitting procedure which gives more weight to central pixels in order to avoid background noise and contamination by neighbor stars. The new PSF is used during the deconvolution process.

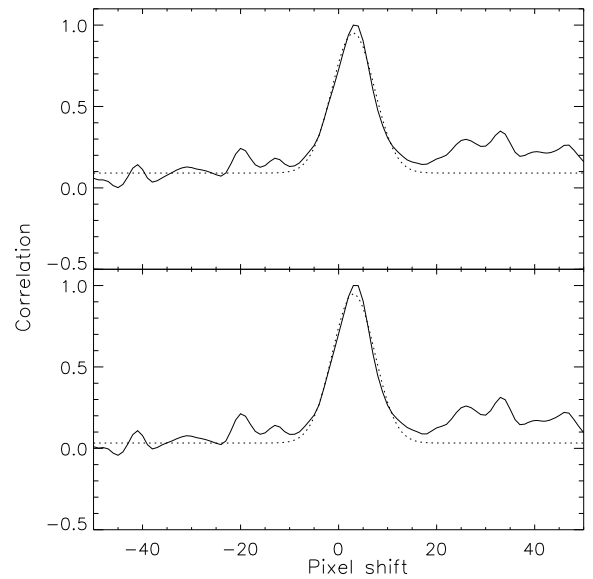


Fig. 8. Cross-correlation function for one of the stars in Baade’s Window field. (Top) Obtained from the velocity measurement of the deconvolved spectrum. (Bottom) Obtained directly from the deconvolution of the CCF data cube. In each case a Gaussian fit has been performed (dotted line). The small differences between both CCF in this example produce output velocities with a difference of 2 km s^{-1} .

Figure 8 shows an example of the CCF from the same star in both cases; the maximum in the deconvolved CCF is found at the same pixel, where each pixel corresponds to 31.78 km s^{-1} . Thus, the deconvolution needs to be run on just a few pixels around the velocity zero channel ($pixel\ shift = 0$) if the expected velocities are not too high (e.g. $|V_r| \leq 300 \text{ km s}^{-1}$). At high spectral resolution the CCF deconvolution could be an interesting way to deblend data cubes spectrally. In spite of the advantages mentioned before, the CCF deconvolution technique was not used in the rest of the article; our radial velocity results are derived from the deconvolution of the data cubes containing stellar spectra.

3.3. Zeropoint velocity corrections

Our data combine three observing runs as Table 2 shows. In order to check the reliability and performance of our technique we repeated in each observing run one of our fields in Sagittarius-I.

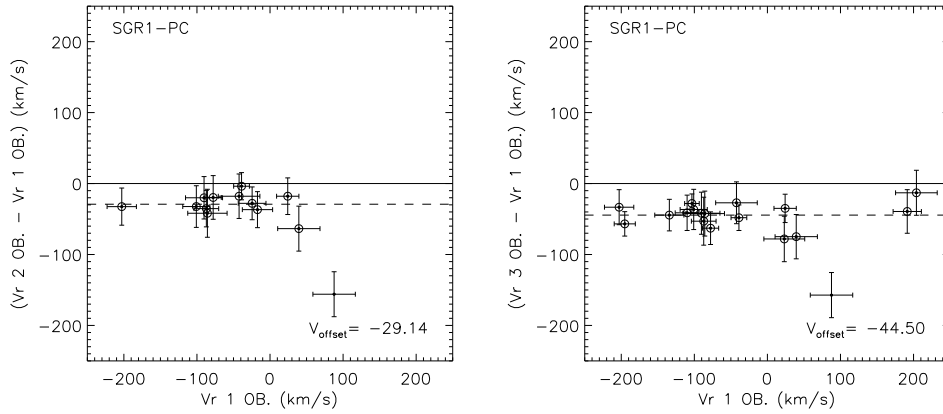


Fig. 9. Velocity zeropoint determination for second and third run IFU fields. IFU field *Sgr1-pc* velocity results have been compared between the first and second observing run (*left*), and first and third (*right*). The fit in each case is iterative, rejecting stars beyond 30 km s^{-1} . Those stars selected in the final iteration are enclosed by a circle.

Table 3. Radial velocity distribution and Gaussian fit parameters for stars with $V_{\text{err}} < 50$.

Field	N_{Star}	$\langle V_r \rangle$ (km s^{-1})	$Stdev$ (km s^{-1})	Kurt	Skew
Sgr-I	773	5 ± 4	119 ± 3	0.004	0.113
Baade's Window	781	8 ± 4	119 ± 3	0.057	0.258
NEAR NGC 6558	563	-14 ± 4	81 ± 4	2.334	0.178
FIELD 4-7	488	19 ± 5	100 ± 5	2.120	0.586
FIELD 3-8	289	2 ± 6	106 ± 8	4.290	1.135
FIELD 10-8 ^a	170(365)	-21 ± 8	98 ± 5	-0.190	0.311
FIELD 10-8 ^b	228(365)	-153 ± 1	30 ± 1	1.468	0.238

Notes. ^(a) Distribution of field stars. ^(b) Distribution from NGC 6656 stars in FIELD 10-8.

Sgr1-pc has a reasonable crowding, with a lack of very bright stars, and represents a typical example of the performance of VIMOS IFU during our bulge observations.

Each year's observations were analyzed with the same HST master list, and reduced independently. Figure 9 shows a comparison of the radial velocities obtained. A significant offset is evident between the observing seasons. Even though the origin of these deviations has not been identified completely, we have corrected them in each case. Accordingly, a zeropoint offset has been added to the observations of the second and third observing runs, 29 ± 11 and 44 ± 8 (km s^{-1}) respectively, where errors have been estimated using 100 000 bootstrap Monte Carlo realizations. These offsets were calculated in each case using an iterative clipping algorithm for all the stars in *Sgr1-pc* field with radial velocities with measured errors below 30 (km s^{-1}). Furthermore, these offsets have been checked against the 5577.5 \AA OI emission line which delivered consistent velocity offsets (28 ± 6 and 38 ± 6 for the second and third epoch respectively). On the contrary, a significant offset was not found for the first epoch. Further proof of the suitability of the applied offsets can be seen in Sect. 4.

4. Analysis

Table 3 and Fig. 10 show our velocity results, where all our velocities are heliocentric and have been corrected to include the zeropoint velocity correction and their respective errors. We only selected ~ 3200 radial velocities for these plots, which correspond to stars with velocity errors $\leq 50 \text{ km s}^{-1}$. Our three minor

axis fields Sagittarius-I, Baade's Window and NEAR NGC 6558, which target denser parts of the bulge, account for the majority of the results (~ 2000 radial velocities), while the rest (~ 1000 radial velocities) are more or less equally distributed between the off-axis fields FIELD 4-7, FIELD 3-8, and FIELD 10-8.

The presence of the cluster NGC 6656 (also known as M 22) on Field 10-8 has been used to check the accuracy of our radial velocity calibrations. Mean radial velocity and dispersion of M 22 are well known and have been checked against our results; Peterson & Cudworth (1994) reported a mean velocity of $-148.8 \pm 0.8 \text{ km s}^{-1}$ and an intrinsic velocity dispersion of $6.6 \pm 0.8 \text{ km s}^{-1}$. The former value is in clear agreement with our reported value of $-153 \pm 1 \text{ km s}^{-1}$. Furthermore, this agreement improves if we limit our sample only to stars with velocity errors below 30 km s^{-1} (126 stars), with a mean velocity of -148 ± 2 .

Similarly, Baade's Window velocities are well documented, and also can be used to assess the accuracy of our results. Hence, we found that Baade's Window and Sagittarius-I have high velocity dispersions in our results, as Table 3 shows. If we constrain once again the sample only to stars with velocity errors below 30 km s^{-1} (621 stars), the dispersion for Baade's Window drops to $112 \pm 3 \text{ km s}^{-1}$ with a mean velocity of $5 \pm 5 \text{ km s}^{-1}$. This measurement shows an excellent agreement with other studies: Babusiaux et al. (2010): $\sigma = 111 \pm 4 \text{ km s}^{-1}$, $\langle V_r \rangle = 9 \pm 6 \text{ km s}^{-1}$, Rangwala et al. (2009): $\sigma = 112 \pm 3 \text{ km s}^{-1}$, $\langle V_r \rangle = 9 \pm 6 \text{ km s}^{-1}$, Rich et al. (2007): $\sigma = 110 \pm 9 \text{ km s}^{-1}$, $\langle V_r \rangle = -1 \pm 13 \text{ km s}^{-1}$, Terndrup et al. (1995): $\sigma = 110 \pm 10 \text{ km s}^{-1}$, $\langle V_r \rangle = -8 \pm 6 \text{ km s}^{-1}$, Sharples et al. (1990): $\sigma = 113_{-5}^{+6} \text{ km s}^{-1}$, $\langle V_r \rangle = 4 \pm 8 \text{ km s}^{-1}$.

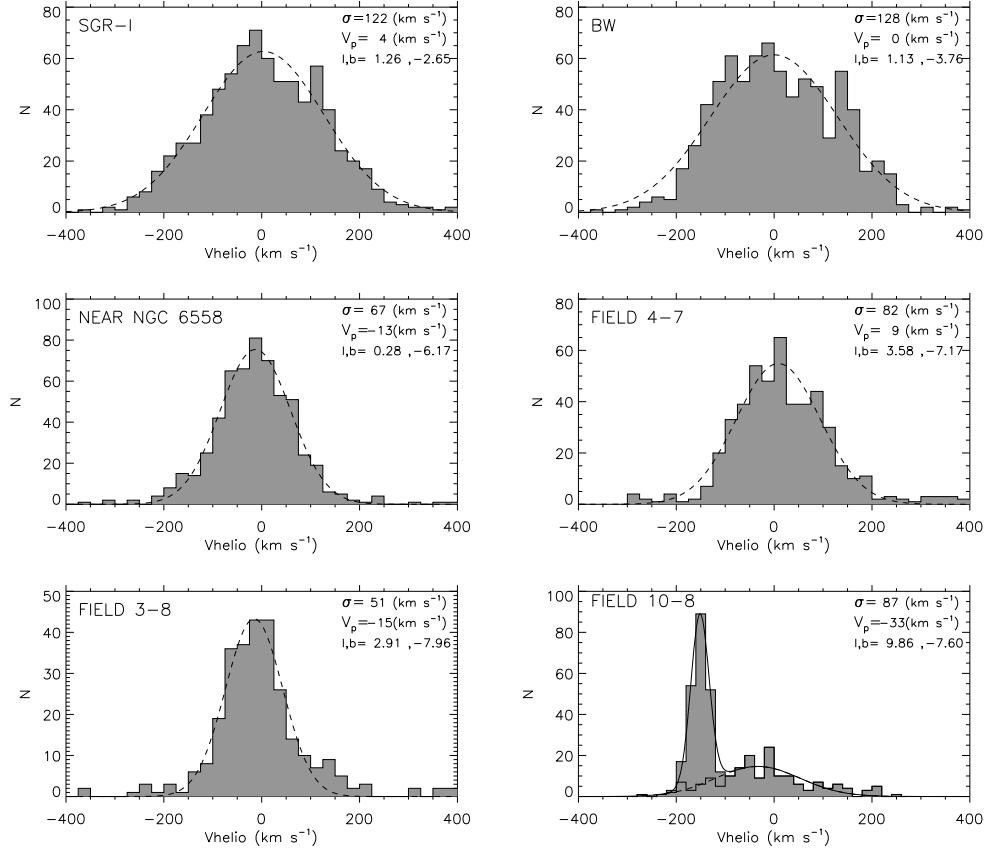


Fig. 10. Velocity histograms for our six fields. A Gaussian fit has been performed in all the cases. Note the contamination by cluster M 22 in Field 10-8, which appears as the narrow peak at ~ -150 km s⁻¹.

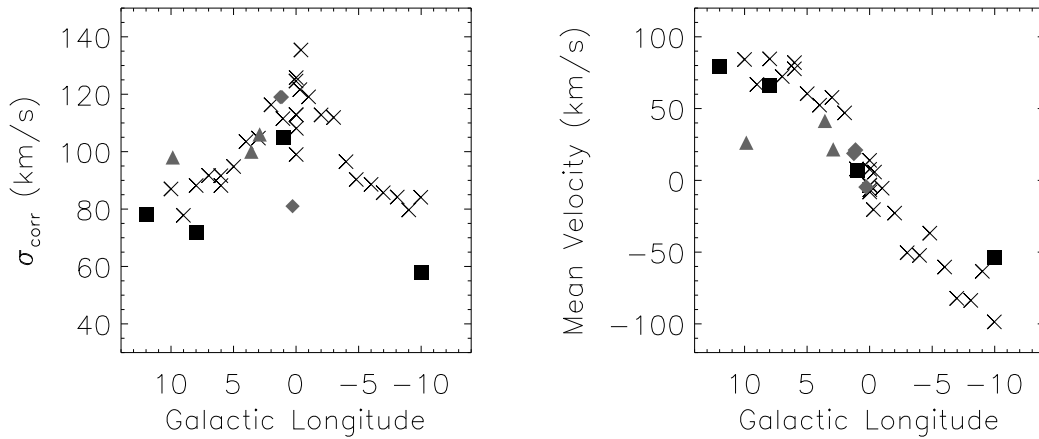


Fig. 11. Velocity dispersion profile σ_{corr} and rotation curve of bulge fields in galactocentric velocity. The plot includes several samples: K-giants by Minniti (1996) (squares), M-giants by Howard et al. (2008) (crosses), and our fields (grey diamonds for minor axis fields and grey triangles for off-axis fields). In some fields we were unable to separate clearly the bulge and disk foreground members (see KR02). This contamination problem was more significant in the fields at positive longitudes and field NEAR NGC 6558.

Kurtosis in the two minor-axis fields, Baade’s Window and Sagittarius-I, are consistent with normal distributions. Conversely, field NEAR NGC 6558 shows a pointy distribution which suggests disk contamination; the same is repeated for Field 4-7 and Field 3-8. Galactic rotation and velocity dispersion curves from previous studies (Fig. 11) and based on K-giants and M-giants at several longitudes (Minniti 1996; Rich et al. 2007, respectively) also show consistency with most of our fields. On the contrary, we found inconsistency in the velocity

dispersion and Galactic rotation curve for Field 10-8 and NEAR NGC 6558 respectively. NEAR NGC 6558 shows a small dispersion compared with the other two minor-axis fields, Sagittarius-I and Baade’s Window, and it is under the curve of velocity dispersion of the galaxy. Nevertheless, NEAR NGC 6558 agrees with the bulge rotation curve. In our off-axis fields we found that Field 4-7 and Field 3-8 seem to show a reasonable agreement with the bulge rotation curve. Field 10-8 on the other hand, does not show a good agreement. This apparent disagreement

in the latter field and NEAR NGC 6558 might be caused by strong contamination by non-bulge stars (mainly cluster stars from M 22 and NGC 6558 respectively), or by poor statistics. Other authors have previously explored contamination rates in Field 10-8 (Minniti et al. 1996).

A key aim of our work is to derive space motions for a large sample of bulge stars, combining radial radial velocities and proper motions. As shown in KR02, main-sequence stars brighter than the turn-off show a proper motion drift consistent with a foreground disk population rotating in front of the bulge, whereas red giants show kinematics representative of the bulge population as a whole. We attempt to remove foreground stars via cuts in the CMD as it is shown in Fig. 12. Unfortunately, no such cuts could be applied to the NEAR NGC 6558 field, for which no suitable archival first epoch images are available, giant and turn-off stars appear saturated on the respective CMD. Hence, proper motions are only available for fainter stars in this field, where we expect disk contamination to be less pronounced at the latitude of this field when compared with the fields SGR-I and Baade's Window. Our three minor-axis fields, whose results we analyze here, SGR-I, Baade's window and NEAR NGC 6558 lie close to the Galactic minor axis. An axisymmetric bulge should produce at those longitudes velocity ellipsoids aligned with the line of sight. Therefore, any deviation of that alignment in the velocity ellipsoid or vertex deviation is a clear signature of a non-axisymmetric bulge. Specifically, a vertex deviation should appear in the correlation of transverse proper motion μ_l and the radial velocity V_r . Although this correlation will be affected by line of sight projection and bulge shape, a significant correlation should be a robust bar indicator. We therefore computed the dispersion tensor σ_{ij}^2 . Eigenvalues and eigenvectors of the dispersion tensor correspond to the axis ratio and direction of the axis of the ellipsoid, while the center is given by the velocity first moments. These calculations have been summarized in Table 4 and plotted in Fig. 13. Values σ_r , σ_l and σ_b are the eigenvalues of the velocity ellipsoid and r_S is the Spearman's correlation coefficient.

The stars shown in Fig. 13 were selected in the CMD with the same cuts as before. An iterative clipping algorithm was used to derive robust dispersions. Figure 13 includes all the iterative velocity ellipsoids, and points within squares are the stars rejected during the process. The values in Table 4 are those found in the last velocity ellipsoid. We find significant correlations in our minor-axis fields; the vertex deviations are virtually the same for the Baade's Window and Sagittarius-I, $-43^\circ \pm 4^\circ$ and $-39^\circ \pm 7^\circ$ respectively, and $-17^\circ \pm 7^\circ$ in NEAR NGC 6558. Similarly the Spearman correlation coefficient r_S shows significant correlations for Baade's Window and Sagittarius-I, the significance ($\text{Prob}(r_S)$) shows a probability over 99.9% that correlations are real in Sagittarius-I and Baade's Window. The latter probability decreases to 90% in the case of NEAR NGC 6558 in agreement with the vertex angle results. Thus, we have a clear trend of a decreasing vertex deviation towards the Galactic plane in the minor-axis which is shown in Fig. 14. These bar signatures even at latitudes of $b \sim -6^\circ$ agree with Shen et al. (2010) N -body simulations of the Galactic bar, where they find bar signatures at $b \sim -8^\circ$. Correlations in the other components of the velocity ellipsoid were also explored. In our sample, the equivalent of the vertex deviation ($l_v = \theta_{lr}$) for the br and lb components (θ_{br} and θ_{lb} respectively) showed no significant correlations for the three minor axis fields.

Even though our selection lacks metallicities, which have been mentioned as a relevant parameter to separate between disk and bulge populations (Minniti 1993; Zhao et al. 1994), the

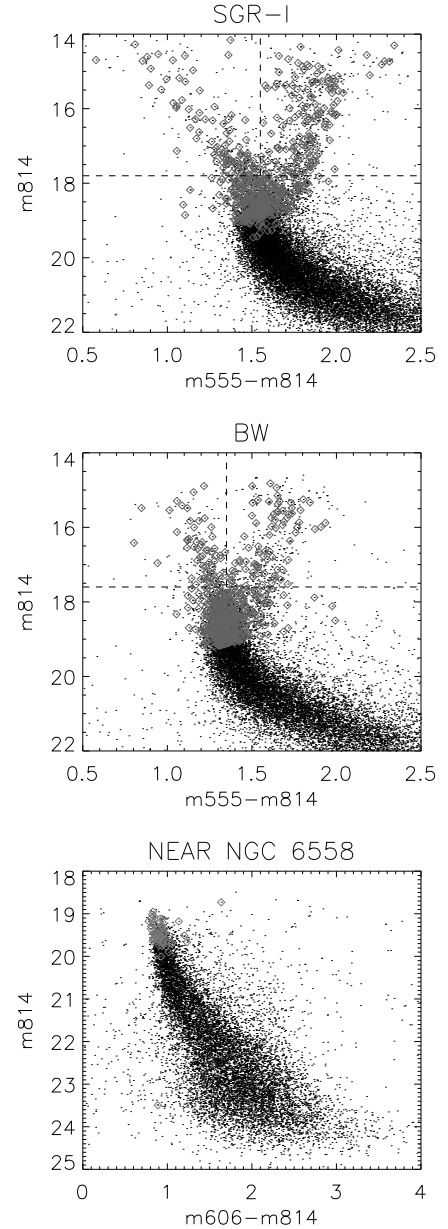


Fig. 12. CMD for the three minor-axis fields. IFU detections (open squares) have been highlighted over HST detections in each field. Dashed lines in Sagittarius-I and Baade's Window fields represent the limits of the different regions in which we have divided each CMD, blue-end of the main sequence (blue-MS; *top left*), red giant branch (RGB; *top right*) and turn-off (*bottom*). Consequently, we have excluded the blue-end of the main sequence from the bulge analysis due to its proper motions; these are consistent with a population dominated by foreground stars rotating in front of the bulge.

agreement with such samples with well established metallicities would support our selection criterion. Zhao et al. (1994) analyzed a subsample of 62 stars with metallicities, radial velocities (Rich 1988, 1990) and proper motions from the original sample of 400 K and M giants by Spaenhauer et al. (1992). In the case of Zhao et al. (1994), only a vertex deviation was found in the metal rich population of his small sample (39 stars). More recently, the original proper motions by Spaenhauer et al. (1992) have been complemented with radial velocity and metallicity measurements (Terndrup et al. 1995; Sadler et al. 1996) allowing

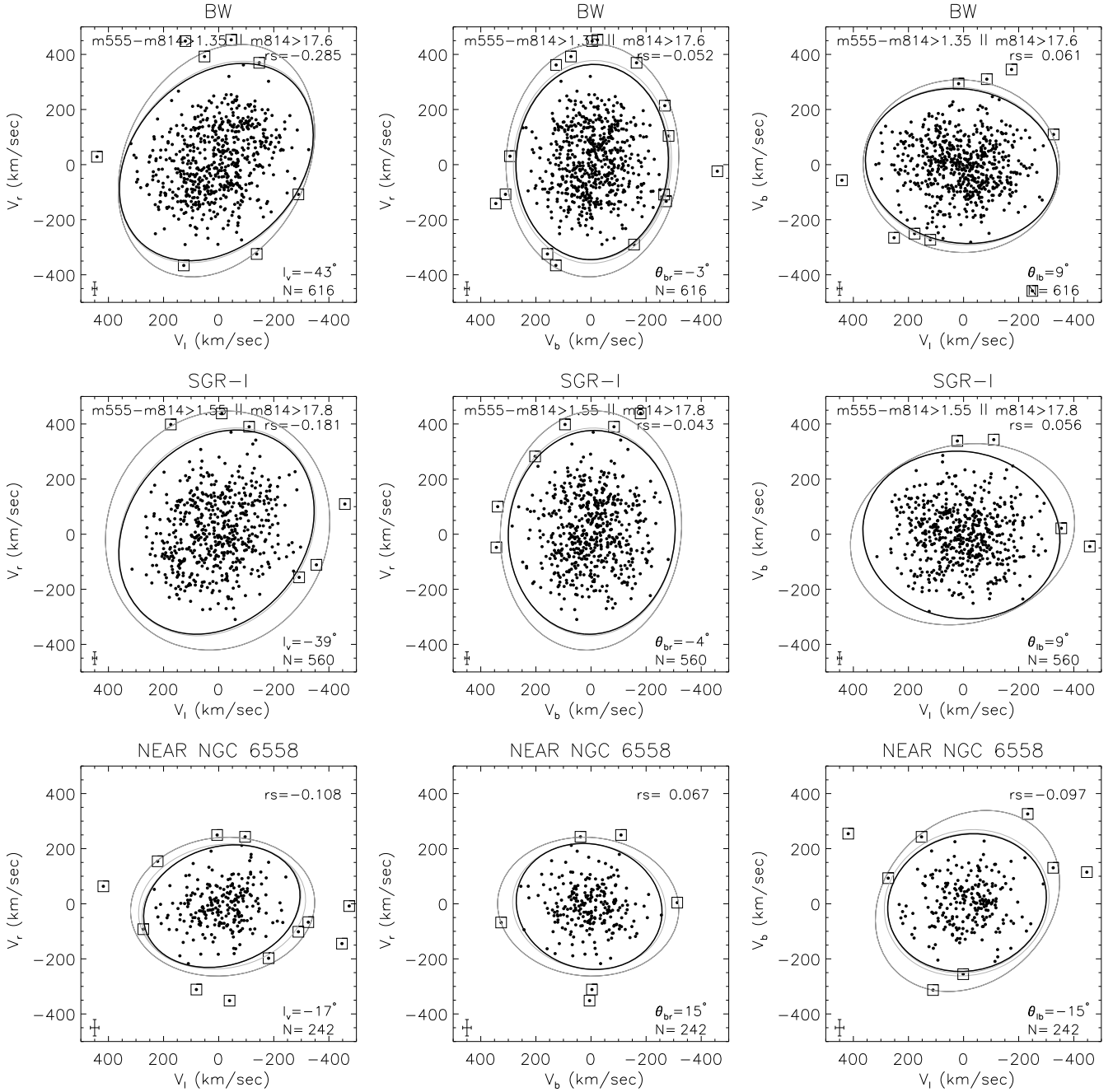


Fig. 13. Velocity ellipsoids for our minor-axis fields. Correlation between V_l and V_r can be related with bulge triaxiality. The color–magnitude selection has been the same shown in Fig. 12 and numbers of the cuts are shown in every plot when present (e.g. for Sagittarius-I the selection is $[m555 - m814 > 1.55 \text{ or } m814 > 17.8]$, which includes turnoff and RGB stars). An iterative clipping algorithm was used to reject stars outside 3.0σ of the velocity ellipsoid to rid the sample of stars with a kinematic behavior different than the majority. Each figure includes all the velocity ellipsoids to illustrate the convergence of the method. Enclosed points are those rejected for the final velocity ellipsoid for which the parameters found have been included in Table 4. In addition, for the final selection has been calculated in each case the Spearman’s correlation coefficient r_s and the vertex angle l_v when possible.

us to have ~ 300 stars with well defined 3-D kinematics and abundances. The result of this increased sample has been consistent with the preliminary Zhao results (Soto et al 2007) showing a significant vertex deviation only for the metal rich stars. Moreover, the sample of K giants shows a remarkable agreement in l_v with our own sample of turn-off and main sequence stars, where the angles found are $-34^\circ \pm 7^\circ$ and $-43^\circ \pm 4^\circ$ respectively. A similar agreement is found for the Babusiaux et al. (2010) sample, with a vertex deviation of $-36^\circ \pm 5^\circ$ in the

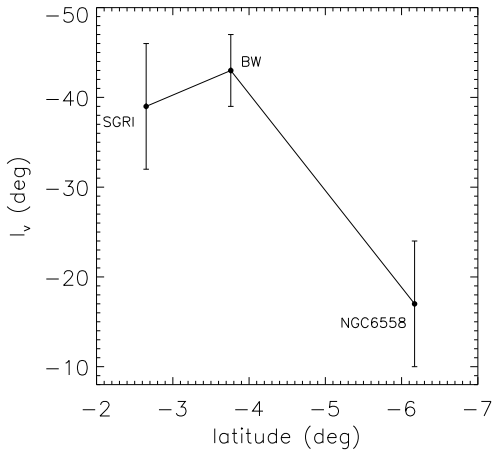
metal rich population. Furthermore, our reported anisotropies in Baade’s Window and Sagittarius-I ($\sigma_b/\sigma_r = 0.89 \pm 0.05$ and $\sigma_b/\sigma_r = 0.85 \pm 0.03$ respectively) also suggest the flattening of the bar population which is consistent with Babusiaux et al. (2010) metal rich population ($\sigma_b/\sigma_r = 0.78 \pm 0.08$). In the same way, we found $\sigma_r \geq \sigma_l > \sigma_b$ for our two fields Baade’s Window and Sagittarius-I.

As an additional exercise, we have explored the velocity ellipsoids for Sagittarius-I and BW, dividing the sample in turnoff,

Table 4. Velocity ellipsoid parameters for Galactic minor-axis fields Baade's Window and Sagittarius-I.

Field	σ_r km s ⁻¹	σ_l km s ⁻¹	σ_b km s ⁻¹	r_s^a	Prob(r_s) ^b	l_v^c (°)	N^d	N_{rej}^e
Sgr-I	121 ± 3	118 ± 3	103 ± 3	-0.181	2e-5	-39 ± 7	560	9
BW	117 ± 3	117 ± 3	104 ± 5	-0.285	5e-13	-43 ± 4	616	10
NEAR NGC 6558	68 ± 4	93 ± 4	90 ± 5	-0.108	0.095	-17 ± 7	242	12
Sgr-I (turn-off)	125 ± 4	118 ± 4	104 ± 4	-0.170	7e-4	-34 ± 6	397	8
Sgr-I (RGB)	111 ± 6	115 ± 6	99 ± 5	-0.200	0.010	-42 ± 9	163	1
Sgr-I (blue-MS)	88 ± 9	114 ± 9	99 ± 8	-0.030	0.782	-14 ± 11	86	3
BW(turn-off)	119 ± 3	117 ± 3	104 ± 6	-0.292	1e-11	-41 ± 6	512	8
BW(RGB)	108 ± 7	114 ± 8	101 ± 6	-0.241	0.014	-40 ± 13	104	1
BW(blue-MS)	94 ± 8	132 ± 10	91 ± 9	-0.149	0.211	-21 ± 7	72	1

Notes. The first three rows correspond to the combination of turnoff and RGB populations which should be dominated by bulge populations (Kuijken & Rich 2002) and according to the cuts in Fig. 12. Last 6 rows are the parameters for the velocity ellipsoids in each field divided by populations, turnoff, RGB and blue MS. ^(a) Spearman's correlation coefficient between μ_l and V_r . ^(b) Prob(r_s) corresponds to the significance of the correlation r_s . ^(c) Vertex angle. ^(d) Total number of stars selected. ^(e) Number of rejected stars during clipping procedure.

**Fig. 14.** Vertex deviation l_v as a function of the Galactic latitude b for the three minor axis fields on this project Sagittarius-I, Baade's Window and NEAR NGC 6558.

blue-end of the main sequence (blue-MS) and red giant branch (RGB). In order to separate into populations, we have used the same limits in color and magnitudes as before to exclude disk stars. Table 4 and Fig. 15 show these ellipsoids. Turnoff selection from the color-magnitude cuts concentrates most of the stars in both samples, repeating the distribution observed in Fig. 13. Similarly, RGB velocity ellipsoids follow the same trend as expected by KR02 binned CMD. At the same time, bright blue main sequence stars show no significant correlation in both fields, where the velocity ellipsoids have converged to vertex angles of $\sim -15^\circ$ as would be expected by a population dominated by foreground stars rotating in front of the bulge. Moreover, the blue-MS velocity ellipsoids show agreement with Babusiaux et al. (2010) metal poor population, σ_l is higher than the other components ($\sigma_r \approx \sigma_b$ in Baade's Window as well). This change in the anisotropy for the blue-MS sample can be related with the combined effect of rotation broadening affecting the μ_l distribution for fields close to the Galactic minor axis (Zhao et al. 1996b) and disk contamination.

All this evidence suggests that our method, even though does not completely isolate the bulge population kinematically, it is very useful to separate regions of the CMD where foreground

disk contamination prevails. Furthermore, the fact that the vertex angle decreases at higher latitudes gives us some clues about the extent of the dynamical influence of the bar feature in the Galactic bulge. We are in the process of incorporating this information into a detailed dynamical model of the bulge/bar.

5. Conclusions

We have described in this paper the procedures and results of a study which aims to identify a significant signature of the stellar bar in several windows with low foreground extinction in the Galactic bulge. Radial velocities have been derived from ~ 110 h of VLT VIMOS-IFU observations.

We have proven that our new method which combines the information from HST photometry, proper motions, and IFU spectroscopy makes feasible the detection of the 3-D kinematics of bulge stars. The radial velocity procedure, based on a deconvolution in the spectral IFU cube using HST positions and a IFU PSF have allowed us to obtain more than ~ 3200 stellar radial velocities.

Our large amount of data, combined with the proper motion information already presented in KR02 and K04, have allowed the detection of a significant vertex deviation in two of our three minor-axis fields. Sagittarius-I and Baade's Window have a significant vertex deviation while a weak signature is observed for the third minor axis field, NEAR NGC 6558. The fact that the bar presents its strongest signature in the first two fields decreasing in the lower latitude field NEAR NGC 6558, delivers valuable information about the extent of the bar feature and must be intrinsically related to the detailed structure of the Galactic bulge.

This project is still in progress. We will soon add proper motions for our three off-axis fields which will complete six fields with radial velocities and proper motions at different locations of the Galactic bulge. Four additional fields with radial velocities and proper motion at negative longitudes have been planned. Thus, our project will sample both ends of the bar obtaining robust constraints in the characteristic bulge parameters. Moreover, a self consistent Schwarzschild model to disentangle the kinematic information in these ten fields is under development. In the end, we expect to determine a detailed picture of the stellar bar and its parameters using the radial velocities and proper motions in our fields.

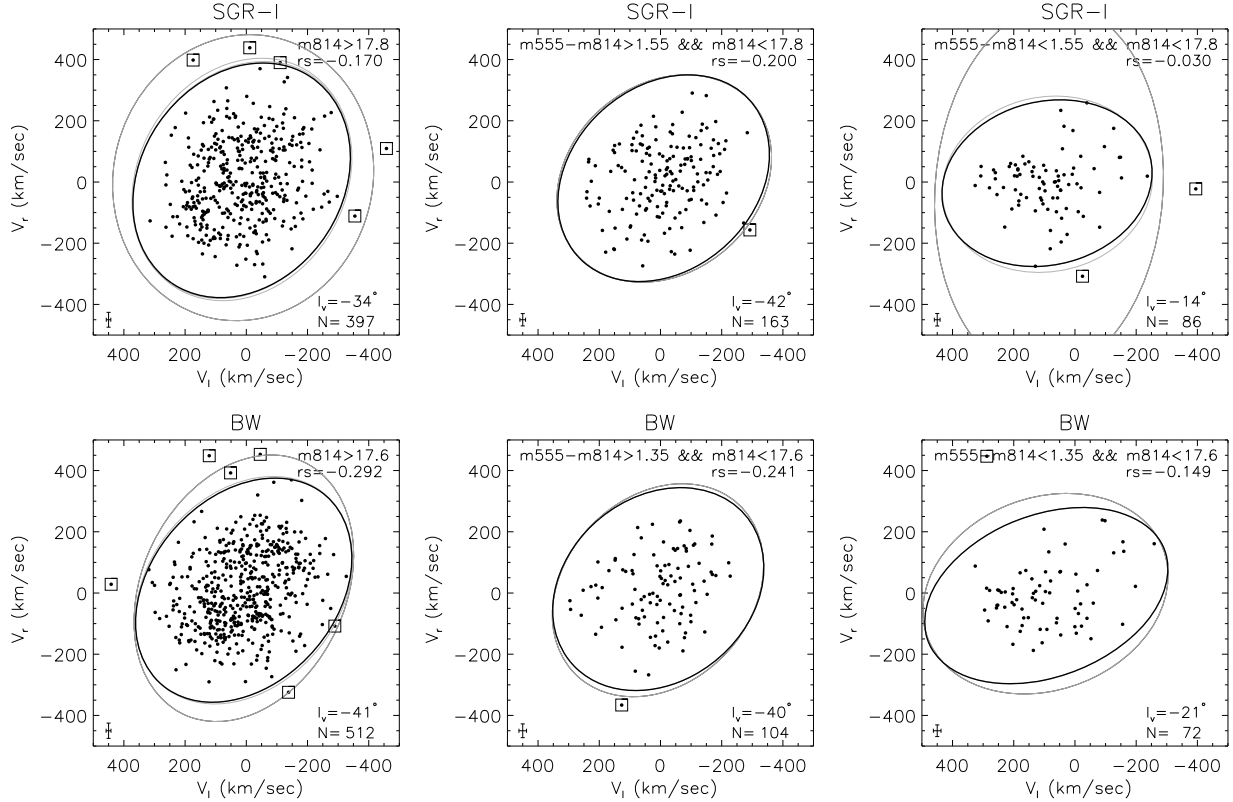


Fig. 15. Baade’s Window and Sagittarius-I velocity ellipsoids for radial velocities (V_r) and transverse proper motion (V_t), divided by population. The region selected is indicated in each plot, and follows the same limits shown in Fig. 12, which correspond (from left to right) to turn-off, RGB and blue-end of the main sequence.

Acknowledgements. We thank Dr. HongSheng Zhao for helpful discussions. Also, we would like to thank the referee of this work for useful comments and suggestions. M.S. acknowledges support by *Fondecyt* project No. 3110188 and Comité Mixto ESO-Chile. Support to R.M.R. for proposals GO-8250, GO-9436, GO-9816 and GO-11655 was provided by NASA through grants from the Space Telescope Science Institute, which is operated by the Association of Universities for Research in Astronomy, Inc., under NASA contract NAS 5-26555.

References

- Anderson, J., & King, I. R. 1999, *PASP*, 111, 1095
Anderson, J., & King, I. R. 2000, *PASP*, 112, 1360
Athanasoula, E. 2005, *MNRAS*, 358, 1477
Babusiaux, C., Gómez, A., Hill, V., et al. 2010, *A&A*, 519, A77
Benjamin, R. A., Churchwell, E., Babler, B. L., et al. 2005, *ApJ*, 630, L149
Binney, J., Gerhard, O. E., Stark, A. A., Bally, J., & Uchida, K. I. 1991, *MNRAS*, 252, 210
Cabrera-Lavers, A., González-Fernández, C., Garzón, F., Hammersley, P. L., & López-Corredoira, M. 2008, *A&A*, 491, 781
Clarkson, W., Sahu, K., Anderson, J., et al. 2008, *ApJ*, 684, 1110
Collinge, M. J., Sumi, T., & Fabrycky, D. 2006, *ApJ*, 651, 197
Cudworth, K. M. 1986, *AJ*, 92, 348
Dwek, E., Arendt, R. G., Hauser, M. G., et al. 1995, *ApJ*, 445, 716
Englmaier, P., & Gerhard, O. 1999, *MNRAS*, 304, 512
Holtzman, J. A., Watson, A. M., Baum, W. A., et al. 1998, *AJ*, 115, 1946
Howard, C. D., Rich, R. M., Reitzel, D. B., et al. 2008, *ApJ*, 688, 1060
Kozłowski, S., Woźniak, P. R., Mao, S., et al. 2006, *MNRAS*, 370, 435
Kuijken, K. 2004, *ASPC 317: Milky Way Surveys: The Structure and Evolution of our Galaxy*, ed. D. Clemens, R. Shah, & T. Brainerd, 310 (K04)
Kuijken, K., & Merrifield, M. R. 1995, *ApJ*, 443, L13
Kuijken, K., & Rich, R. M. 2002, *AJ*, 124, 2054 (KR02)
Martinez-Valpuesta, I., & Gerhard, O. 2011, *ApJ*, 734, 20
McWilliam, A., & Rich, R. M. 1994, *ApJS*, 91, 749
McWilliam, A., & Zoccali, M. 2010, *ApJ*, 724, 1491
Mellinger, A. 2008, *Star Forming Regions along the Milky Way: A Panoramic View*, in *Handbook of Star Forming Regions*, ed. B. Reipurth, Vol. I (ASP)
Minniti, D. 1993, *IAUS 153: Galactic Bulges*, ed. H. DeJonghe, & H. Jan Habing, 315
Minniti, D. 1996, *ApJ*, 459, 175
Nataf, D. M., Udalski, A., Gould, A., Fouqué, P., & Stanek, K. Z. 2010, *ApJ*, 721, L28
Peterson, R. C., & Cudworth, K. M. 1994, *ApJ*, 420, 612
Picaud, S., & Robin, A. C. 2004, *A&A*, 428, 891
Rangwala, N., Williams, T. B., & Stanek, K. Z. 2009, *ApJ*, 691, 1387
Rattenbury, N. J., Mao, S., Debattista, V. P., et al. 2007a, *MNRAS*, 378, 1165
Rattenbury, N. J., Mao, S., Sumi, T., & Smith, M. C. 2007b, *MNRAS*, 378, 1064
Rich, R. M. 1988, *AJ*, 95, 828
Rich, R. M. 1990, *ApJ*, 362, 604
Rich, R. M., Reitzel, D. B., Howard, C. D., & Zhao, H. 2007, *ApJ*, 658, L29
Sadler, E. M., Rich, R. M., & Terndrup, D. M. 1996, *AJ*, 112, 171
Saito, R. K., Zoccali, M., McWilliam, A., et al. 2011, *AJ*, 142, 76
Sharples, R., Walker, A., & Cropper, M. 1990, *MNRAS*, 246, 54
Shen, J., Rich, R. M., Kormendy, J., et al. 2010, *ApJ*, 720, L72
Spaenhauer, A., Jones, B. F., & Withford, E. 1992, *AJ*, 103, 297
Schwarzschild, M. 1979, *ApJ*, 232, 236
Soto, M. 2010, Ph.D. Thesis, Leiden Observatory
Soto, M., Rich, R. M., & Kuijken, K. 2007, *ApJ*, 665, L31
Schwarzschild, M. 1982, *ApJ*, 263, 599
Terndrup, D. M., Rich, R. M., & Sadler, E. M. 1995, *AJ*, 110, 1774
Tonry, J., & Davis, M. 1979, *AJ*, 84, 10
Zhao, H. S. 1996, *MNRAS*, 283, 149
Zhao, H. S., Spiegel, D. N., & Rich, R. M. 1994, *AJ*, 108, 2154
Zhao, H. S., Rich, R. M., & Spiegel, D. N. 1996a, *MNRAS*, 282, 175
Zhao, H. S., Rich, R. M., & Biello, J. 1996b, *ApJ*, 470, 506
Zoccali, M., Lecœur, A., Barbuy, B., et al. 2006, *A&A*, 457, L1